A New Distorted Circle Estimator using an Active Contours Approach

Fabrice MAIRESSE, Tadeusz SLIWA, Yvon VOISIN and Stéphane BINCZAK

Université de Bourgogne, Le2i UMR CNRS 5158
Route des plaines de l'Yonne, BP 16, 89010 Auxerre, France
Phone number: 33 (0)3 86 49 28 53 – Fax number: 33 (0)3 86 49 28 50
{Fabrice.Mairesse, Tadeusz.Sliwa, Yvon.Voisin, stbinc}@u-bourgogne.fr

Abstract. A new circle estimator is proposed for solving heavy subpixel error on circle center in the case of noticeable distortion. It is based on an innovative point of view over active contours process blending mathematical morphology and electronic phenomenon that furnishes a multi-level image in a single pass from the approximated form of objects to a full detailed one. A comparison with least-mean squares method supports that a sensitive improvement can be obtained compared to a more classic method.

Keywords: Discrete circles, geometric noise, Radon transform, model fitting, active contours

1 Introduction

Active contours have been developed to overpass the limitations of classic segmentation tools as filtering, for example, leads to problems of segmentation as unconnected or incomplete contour, notably due to contrast variation, difficulty to find optimal parameters, noise, etc. Active contours are one of the best known and widely used solution to avoid these problems. The limitation of these methods is to give a unique representation of the form that can be assimilated at the scale of the representation, only allowing to have n scale representation at the price of n computation cycles. Contrariwise, mathematical morphology [1], [2] furnishes a tool that corresponds to this idea of multi-scale representation. Geodesic dilation is one of the basic mathematical morphology techniques, related to geodesic reconstruction and watershed algorithm. Although mainly numerical implementations of these techniques are available for usual real time applications [3], [4], an intuitive interpretation of these operations allows high speed imaging. A known limit of geodesic operators is that they do not take into account the regularity of the shape of the objects. But, the second connexity notion, developed by J. Serra in [2], leads to consider non-adjacent objects as being connected. In this context, the authors have decided to explore a possible generalization to the regularity of the shape of the objects. Authors have also noticed that another aspect is very important for the notion of objects' regularity: The scale from which the object is observed but multiscale analysis needs multiple wave propagation. In order to be compatible with high speed imaging, authors have studied a phenomenon producing propagation of wavefronts that have an increasing regularity along the height of the transition part. It is presented in the following section.

2 Active Contours

Let us consider a bidimensional regular discrete (N,M) length grid Ω on which the following bistable diffusive system is defined:

$$\frac{dv_{n,m}}{dt} = D_{n,m}\left[v_{n-1,m} + v_{n+1,m} + v_{n,m-1} + v_{n,m+1} - 4v_{n,m}\right] - v_{n,m}\left(a - v_{n,m}\right)\left(1 - v_{n,m}\right) \ . \tag{1}$$

where $D_{n,m}$ is a local diffusion parameter and a, a threshold parameter.
The system is completed by the Neumann conditions (zero-flux conditions) on the border $\partial\Omega$ of the definition domain Ω, so that:

$$\frac{\partial v_{n,m}}{\partial \eta} = 0 \ \ if \ \ (n,m) \in \partial\Omega \ . \tag{2}$$

where $\partial/\partial\eta$ denotes the outer derivative boundary.
The study of this system leads the authors to consider the emerging propagation phenomena over homogeneous and inhomogeneous grid cases to deduce a generic image processing method.

2.1 Homogeneous Grid Case

In order to simplify, the local diffusion parameter is considered as a constant

$$D_{n,m} = D \ \forall(\mathrm{n,m}) \in \Omega \ . \tag{3}$$

This is a discrete version of the FitzHugh-Nagumo partial differential equation (PDE). In the uncoupled case, i.e. when $D=0$, $v_{n,m}=0$ and $v_{n,m}=1$, $\forall\{n,m\}$ are two attracting steady states, while $v_{n,m}=a$, $\forall\{n,m\}$ is an unstable equilibrium point of the system, acting as a threshold. In case of strong coupling, i.e. when D is large, we expect that a traveling wave will propagate depending on the value of a with a constant speed so that if $a<½$ ($a>½$ resp.), the steady state $v=1$ ($v=0$ resp.) will propagate at the expense of the steady state $v=0$ ($v=1$ resp.). When $a=½$, no propagation occurs.
The response system also depends on initial conditions. For example, a marker, defined by $v_{i,j}(t=0)=1$ for a set of (i,j) values and $v_{k,l}(t=0)=0$ otherwise, imposes the kind of traveling waves due to its symmetry. The two main propagating structures are the planar and the circular wavefronts.

Planar Waves. They emerge from a rectangular marker (Fig. 1-A) where two planar wavefronts propagate in opposing directions. Such propagation reduces the system to a one-dimensional problem that gives us:

$$\frac{dv_n}{dt} = D\left[v_{n-1} + v_{n+1} - 2v_n\right] - v_n\left(a - v_n\right)\left(1 - v_n\right) \ . \tag{4}$$

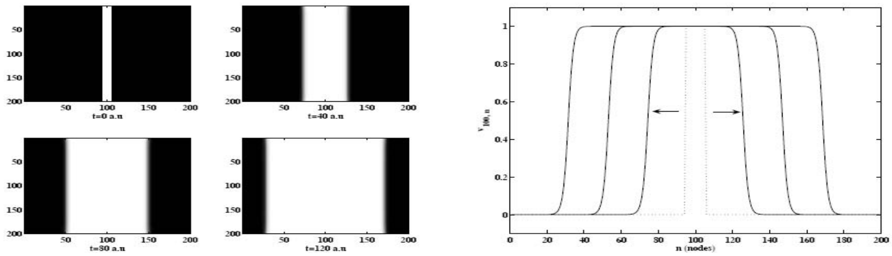

Fig. 1. A) A planar wavefront propagation using a grayscale representation where white corresponds to *v=1* and black *v=0*. Top left inset shows the marker. Other insets illustrate the propagating wavefronts at different times in a.u. (arbitrary units). B) $v_{100,n}$ at different times corresponding to the insets of Fig1.a), illustrating the constant velocity. Dot line: marker, continuous lines: propagating wavefront at *t=40*, *80* and *120* a.u.. Parameters: *a=0.1*, *D=1*.

This system has been widely studied and some important results can allow us to characterize the process of propagation, although no explicit overall analytical expression of the wavefronts is available. Among these results, the differential-difference can be written in a case of strong nodes coupling, using continuum approximation:

$$\frac{\partial v}{\partial t} = \Delta v - v(v-a)(v-1) \ . \tag{5}$$

Where Δ is the laplacian operator. A traveling-wave analysis allows us to express the traveling wave profile, considering initial conditions ξ_0 and $\xi = n - ut$, and its velocity u:

$$v(\xi) = \frac{1}{2}\left[1 \pm \tanh\left[\frac{\xi - \xi_0}{\sqrt{8aD}}\right]\right] . \tag{6}$$

$$u = \pm(1-2a)\sqrt{\frac{D}{a}} \ . \tag{7}$$

In equation (6), one can notice the inverse relation between D and the width of the wavefront that remains true even in a discrete system. Equation (7) highlights the importance of the parameter a value compared to ½ and that the velocity increases when a decreases. The ± symbol in equation (7) corresponds to the bidirectional propagation. These remarks stay qualitatively valid in the discrete case.
Moreover, a major feature due to discreteness is the failure of the propagation when D is smaller that a critical non-zero value $D^* > 0$, which is missed in the continuum approximation. In this case, the wavefront is pinned [5, 6]. From [6], an asymptotic expression of this parameter when $a \to 0$, is

$$D^* = \frac{1}{4}a^2 \ . \tag{8}$$

Circular Waves. Circular waves emerge from a circular or almost circular marker or from a marker containing a circular symmetry as illustrated in figure 2.

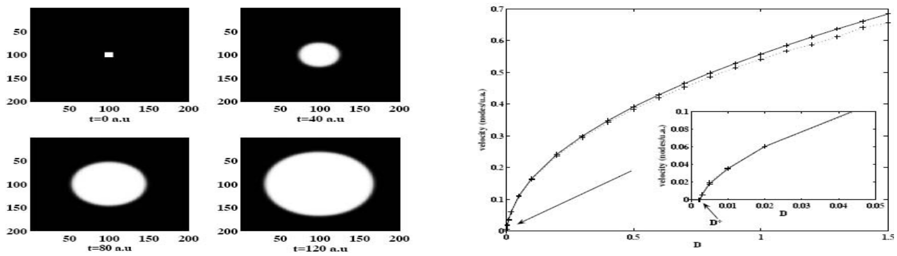

Fig. 2. A) A circular wavefront propagation using a greyscale representation where white corresponds to $v=1$ and black $v=0$. The top left inset shows the marker. The other insets illustrate the propagating wavefronts at different times in a.u. (arbitrary units). B) Propagation velocity versus the diffusive parameter D. Numerical results comparison between planar wave speed (continuous line) and circular wave speed (dot line). Parameter $a = 0.1$.

The spatial shape determines the velocity of the wavefronts, so that, in a continuous system [7], a convex traveling wave propagates slower than a planar one. This comportment is verified as it can be seen in the comparison between planar wave speed and circular wave speed when D increases (Fig. 2). When D decreases, the circular propagation is replaced by a multi-planar propagation with different wave vectors as the wavefront width becomes smaller and is confronted to the discreteness of the system. That is to say that for, a small value of D, planar and circular wavefronts are merged. In addition, propagation fails for the same value D^* of D. From now on, we will assume that D^* is not a function of the kind of traveling waves, but only determined by the threshold parameter a.

2.2 Inhomogeneous Grid Case

Contrary to the homogeneous grid case, the point of interest is the blocking case. Indeed, it allows the control of the path of the topological traveling wave. An image is then defined as a discrete bi-dimensional grid where nodes correspond to pixels sites. Each node is coupled to its nearest neighbors in a diffusive manner weighted by the local intrinsic information of the image. The main idea is to initiate a wavefront and let it propagate until it reaches an object Θ to be detected. In order to prevent further propagation, we now impose the following rule:

$$D_{n,m} = \begin{cases} D_p > D^* \; if \quad (n,m) \notin \Theta \\ 0 \qquad\qquad otherwise \end{cases} . \qquad \textbf{(9)}$$

I.e. the wavefront cannot propagate in the object (D=0) and is limited to the borders of Θ. Contrariwise, the propagation is possible since the marker (or a part of the marker) is outside the object ($Dp>D^*$) (Fig. 3-A). The relationship between the diffusive parameter D, the width W and the thickness T of the corridor has been studied and is presented in Fig. 3-C. A critical value, Dm, of the diffusive parameter leads to a no propagation of the wavefront (Fig. 3-B). Obviously, the larger and thicker the corridor is, the wider a propagating wave can be, therefore, *Dm* increases. As discussed in the following section, this property can be interesting to integrate objects or to develop active curves.

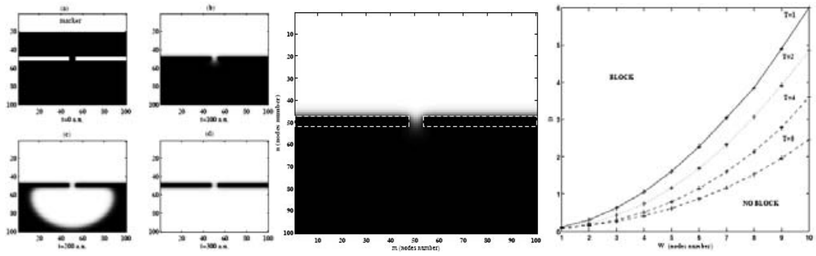

Fig. 3. A) Propagation of a wavefront in an inhomogeneous grid. Inset (a) shows the initial marker and an object Θ. Inset (b) shows the wave front crossing the corridor separating the two parts of Θ at *t=100* a.u.. Inset (c) shows the propagation of a circular wave emerging from the corridor at *t=200* a.u.. Inset (d) shows the final stationary state, obtained at *t=300* a.u.. B) Unsuccessful propagating wave (D = 1.2) C) Diffusive parameter D versus width W; curves for different values of thickness T of Θ. When D is above this curve, the wavefront is pinned. When D is beneath this curve, the wavefront can cross the corridor and propagate. Parameters: *a=0.1*, *D=1*, *W=6 nodes*, *T=4 nodes*.

2.3 A Generic Image Processing Method

Let *A* and *B* denote sets or indicate sets functions or even grayscale image quantities as scalar-type results of some image processing (for example, linear filtering). A and *B* can derive from the same image or from different images. Here *A* represents binary marker from which a propagation phenomenon starts from, and *B* a topological constraint derived from the image. The couple of scalar discrete functions (*A*,*B*) defines the following equation:

$$E_\varepsilon(A,B):\left\{\begin{array}{c}\dfrac{dv_{n,m}}{dt}=\dfrac{D(B)}{\varepsilon}(v_{n-1,m}+v_{n+1,m}+v_{n,m-1}+v_{n,m+1}-4.v_{n,m})-f_a(v_{n,m})\\ with\, f_a(v)=v(a-v)(1-v)\; for\; a<\dfrac{1}{2},\\ D(B)=\dfrac{1+\tanh(20.B-12)}{2},\; and\; v\,|_{t=0}=A\end{array}\right\}. \quad (10)$$

With *a=0.1* and the definition domain *Ω* being the *(n,m)−length* grid. The system is completed by the Neumann conditions. A marker-rule is set so that the marker remains constant and equal to 1. This choice of constructing *D(B)* corresponds to a bimodal distribution of the local diffusive parameter separated by *D**, allowing the control of the propagating paths. The propagation phenomenon defined by *E* tends to a convergence state noted $v_\varepsilon^\infty(A,B)$, theoretically corresponding to infinite *t* but practically a millisecond value will be sufficient in most cases. Then, let us define the main image processing operator as:

$$\Phi\varepsilon,h(A,B) = \{v_\varepsilon^{\infty}(A,B) \geq h\}\ . \tag{11}$$

The propagation phenomenon is similar to the geodesic propagation, but with an additive scale of regularity constraint, defined by the couple variables (ε,h) with ε defining the magnitude order of the scale of regularity of the one-pass propagation and h a thresholding along the scale regularity consequently to the choice of ε in the final result when the propagation is definitively blocked by the topological constraint. It is equivalent to fix ε and deduce h or to fix h and deduce ε. Eq. (11) leads to the immediate following properties:

• When $\varepsilon^{-}\rightarrow 1+/D^*$, $\Phi_{\varepsilon,h}(A,B)$ tends to the geodesic reconstruction of B marked by A.

• $\Phi_{\varepsilon,h}(.,B)$ is increasing with fixed regularity scale parameters and increasing with its two regularity scale parameters increasing independently.

• $\Phi_{\varepsilon,h}(A,\ .)$ is decreasing with fixed regularity scale parameters and decreasing with its two regularity scale parameters increasing independently.

It allows the generation of many morphological-type analysis techniques, constructed as classic techniques through the morphological theory, but with some advantages from the point of view of active curves (considering the evolving front) or regions (considering the interior of the evolving curve) as their greater regularity, without the topological problems of the deformable templates. As illustrated by the experimental study, ε plays the rule of a main geometric scale parameter and h a secondary geometric scale parameter. The > sign produces an active geodesic region approach, < producing a dual region approach, whilst replacing it by = produces an active geodesic curve approach. For the following paragraph, c represents $^{1}/\varepsilon$.

One of the main advantages that has not been illustrated is the one-pass multi-scale approximation. Considering the shape of figure 4, the propagation of the traveling wave has a comportment of viscous gauge (Fig. 4). Analyzing the grayscale resulting image gives us a set of multi-scale representations of the original shape (Fig. 5). Low thresholds give higher details and high thresholds furnish higher approximation of the shape. At limit of the domain of the image, i.e. in our case [0, 1], we obtain almost the initial shape for low threshold (~0) and approximation hulls for high threshold (~1).

Fig. 4. Scale aspect: Hull effect (with inner and outer markers). Left: final state. Right: Shape and marker. Parameter c = 8.

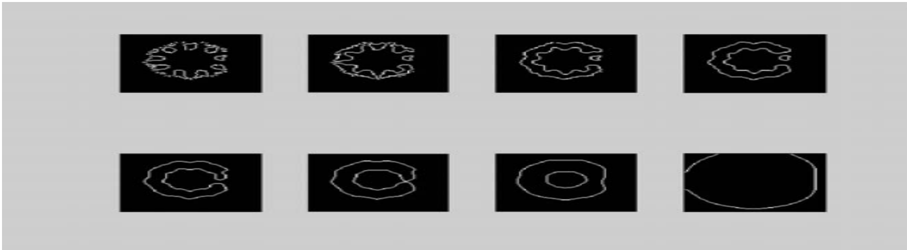

Fig. 5. Secondary geometrical scale aspect of h. From left to right, then top to bottom, h increases in a ratio-2 geometrical manner from h = 0.0078 to h = 0.996. Parameter: c = 8.

The figure 6 illustrates the effect of blockage depending on *c*. The more *c* increases, the less propagation penetrates in the porous medium. It works as if the propagation becomes more viscous. It could be interpreted as if each elementary part of the propagation front was blocked by a virtual dilation whose size is determined by the scale *c*. Therefore, *c* can also be denoted as the "scale of observation". This phenomenon is useful for noised circles centre determination.

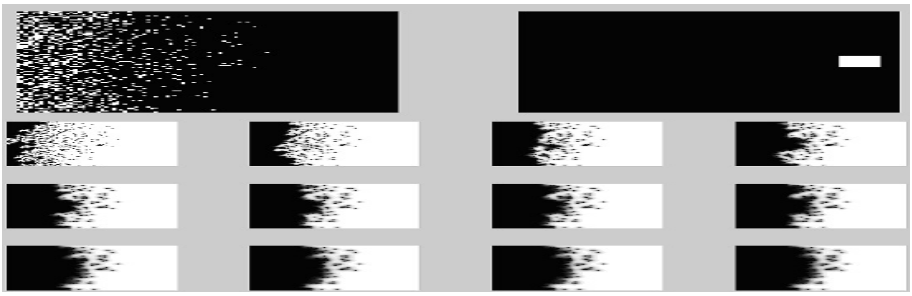

Fig. 6. Scale aspect of c: Porosity effect (up: shape and marker, down: propagation blockage for increasing values of c from left to right and up to bottom: c = 0.1 to c = 1.75 by incremental steps of 0.15)

3 Applications to Circles

3.1 Samples

A valuable application of these concepts is the measurement of circles, especially distorted ones. Indeed, an active contours approach of a distorted circle can lead to the obtainment of a more circular form (Fig. 7). So we consider a test set produced by modeling a certain variety of perfect and imperfect discrete circles. Circles coordinates are described by:

$$\left\{x = E\left[x_0 + r\cos(\theta)\right], y = E\left[y_0 + r\sin(\theta)\right]\right\} . \quad \textbf{(12)}$$

E[x] being the nearest integer of *x*.
Noise and distortion can be added to those circles by modifying the radius:

$$\left\{\begin{matrix} r \longrightarrow r - A_{noise} \\ r \longrightarrow r - a_{distortion} \end{matrix}\right\}. \qquad \textbf{(13)}$$

with A_{noise} a random variable of centered Gaussian density of probability and $a_{distortion}= a|sin(\theta)sin(\alpha\theta)exp(-\beta\ (\theta+\pi^4))|$, a, α and β representing parameters of this deformation.
With varying values of $x0$, $y0$ and r, we obtain a statistically significant set of test images to distinguish our measurement tools. Typically, noise and distortion amplitude are respectively set to 5 and 10 (Fig. 8). The relative scale unit is the pixel one.

Fig. 7. Left: initial image and final active contours image, Right: several thresholds of the final active contours image (i.e. several views at different scale)

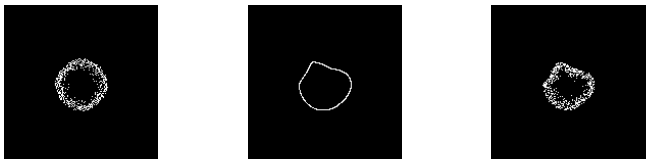

Fig. 8. Left: noised circle, Middle: distorted circle, Right: noised and distorted circle

3.2 Radon Based (*RB*) Method

The main idea of the method is to describe a circle by its tangents to access to circle radii. Indeed, three tangents i.e. three points are sufficient to compute circle characteristics and only two if we consider parallel tangents. The authors' approach is to compute radii from those tangents and determine circle center by their intersection. Considering a discrete framework, each arc of the circle can be considered as a segment at a certain scale. Thereby, a discrete tangent can pass through one and, generally, several pixels.
That is why the authors use the Radon transform to find tangents [8]. As the Radon transform converts an image (x,y) into a new domain (ρ,θ), it is obvious to isolate the lines which include the most of pixels because they correspond to maxima in the upper and lower parts of the signal. Although these lines do not always correspond to tangents, they are even so neighboring. In the continuation, these lines are considered as circle tangents.
The first step is to find each couple of tangents at the discrete angle θ_i (θ_i Є [0, pi[). To that end, the Radon transform is separated into two parts at the level of the

barycenter for all discrete angles to obtain the upper and lower parts of the original signal. This allows to correctly identify each maximum in each part of the signal.
Once these maxima found, radii can be computed by considering the mean of the parameter ρ of the tangents for each θ_i in the Radon domain. For simplification purpose, the value of that point is set to the mean of maxima. To enhance results, a fitting is done on data considering the parametric representation of an image point, here the circle center, in Radon domain.
The authors use a trust region algorithm [9] for nonlinear least mean squares. To improve the fitting, it is necessary to suppress unlikely points that imply a loss of precision when noise or distortion is added. The implemented method is an iterative $\alpha.\sigma$ method where α decreases along iteration. In order to have the radius of the circle, a mean of the distance between each tangent is done.

3.3 Results

To have a point of comparison, the authors use a classic least-mean squares (LMS) method for circles [10]. Results are presented in the tables 1 and 2. Both methods have been applied on initial simulated circles, then on edge of several threshold (i.e. several scale) of the active contours results. The first conclusion is that the RB estimator is not adapted for perfect or noised circles. It only takes its interest in the case it is made for, that is to say the distorted circles. One can see that the active contours method does not significantly affected the precision of least mean square estimator. In the same way, even if an increase of precision is visible, it is only significant for distorted circles as heavy distortions are compensated. The difference of precision reaches nearly 1.5 pixel in distorted cases and nearly 0.84 pixel in noised and distorted cases in favor of RB estimator with a threshold of 128 and eight or the nine iterations.

Table 1. Mean error of the least mean squares method

Mean error of the least mean squares method on circle center position (given in pixel)					
	Threshold	Perfect circle	Noised circle	Distorted circle	Noised & distorte circle
Initial image		0,014744	0,13226	2,1681	2,2607
Active contours	2	0,022057	0,127	2,1448	2,0067
	4	0,022057	0,12014	2,1448	2,0286
	8	0,022057	0,11924	2,1448	2,0472
	16	0,022057	0,11253	2,1448	2,0727
	32	0,022057	0,11003	2,1448	2,0938
	64	0,025468	0,10829	2,1367	2,1188
	128	0,025539	0,11306	2,1377	2,1219

Table 2. Mean error of the Radon based method

Mean error of the Radon based method on circle center position (given in pixel)					
	Threshold	Perfect circle	Noised circle	Distorted circle	Noised & distorte circle
Number of iterations needed		0 iteration	2 iterations	8 iterations	9 iterations
Initial image		0,44724	0,52831	1,5025	2,8024
Active contours	2	0,40452	0,37137	0,77922	1,7336
	4	0,40452	0,36452	0,77922	1,643
	8	0,40452	0,34141	0,77922	1,6091
	16	0,40452	0,41065	0,77922	1,4555
	32	0,40452	0,33302	0,77922	1,5274
	64	0,31284	0,35953	0,69957	1,2991
	128	0,3853	0,34013	0,64396	1,1671

4 Conclusion

This paper has contributed a new approach for problems of circles measurement in a heavy distorted context. It consists on an active region algorithm that is able to furnish a multi-leveled image of a contour in a single pass combined with a Radon transform based estimator. Levels are defined by a granularity parameter that allows to focus on a particular scale. A more circular form can be obtained at a larger scale even if an error on the diameter is introduced. The circle estimator, resting on an approach of the circle by its tangents, furnishes a subpixel approximation of the center thanks to a fitting in the Radon parameter domain. Results, compared to various classic methods, show the adequacy of a pre-processing by a propagation of wavefronts combined with a tangential approach for measurement on distorted circles.

References

1. Serra, J.: Image Analysis and Mathematical Morphology Vol. I. London: Academic Press. (1982)
2. Serra, J.: Image Analysis and Mathematical Morphology Vol. II : Theoretical Advances. London: Academic Press. (1988)
3. Goldenberg, R., Kimmel, R., Rivlin, E., Rudzsky, M.: Fast Geodesic Active Contours. IEEE Trans. Image Proc., Vol. 10 (10). (2001) 1467–1475
4. Paragios, N., Deriche, R.: Geodesic Active Contours and Level Sets for the Detection and Tracking of Moving Objects. IEEE Trans. PAMI, Vol. 22 (3). (2000) 266– 80
5. Keener, J.: Propagation and its failure in coupled systems of discrete excitable cells. ISIAM J. Appl. Math., Vol. 47 (3). (1987) 556–572
6. Erneux, J., Nicolis, G.: Propagating waves in discrete bistable reaction-diffusion systems. Physica D, Vol. 67 (3). (1993) 237–244
7. Fast, V.G., Kleber, G.: Role of wavefront curvature in propagation of cardiac impulse. Cardiovascular research, vol. 33. (1997) 258–271
8. Kim, H., Kim, J.: A two-step circle detection algorithm from the intersecting chords. Pattern recognition letters, 22. (2001) 787-798
9. Branch, M.A., Coleman, T.F., LI, Y.: A subspace, interior, and conjugate gradient method for large-scale bound-constrained minimization problems. SIAM Journal of scientific computing, 21(1). (1999) 1-23
10. Chernov, N., Lesort, C.: least-squares fitting of circles and lines. Computer vision and pattern recognition. (2003)